Observation of preferential sputtering of Si/graphite anodes from Li-ion cells by GD-OES and its validation by neutron depth profiling

Ivana Pivarníková [a,b,1], Marius Flügel [c,1], Neelima Paul [a,*], Antonino Cannavo [d], Giovanni Ceccio [d], Jiří Vacík [d], Peter Müller-Buschbaum [a,b], Margret Wohlfahrt-Mehrens [c,e], Ralph Gilles [a], Thomas Waldmann [c,e]

[a] Heinz Maier-Leibnitz Zentrum (MLZ), Technical University of Munich, Lichtenbergstr.1, 85748, Garching, Germany
[b] Technical University of Munich, TUM School of Natural Sciences, Department of Physics, Chair for Functional Materials, James-Franck-Str. 1, 85748, Garching, Germany
[c] ZSW – Zentrum für Sonnenenergie- und Wasserstoff-Forschung, Baden-Württemberg, Helmholzstraße 8, 89081, Ulm, Germany
[d] Nuclear Physics Institute, Academy of Sciences of the Czech Republic, CZ-25068, Řež, Czech Republic
[e] HIU - Helmholtz Institute Ulm for Electrochemical Energy Storage, Helmholtzstrasse 11, 89081 Ulm, Germany

Keywords:
Lithium-ion batteries
Neutron depth profiling (NDP)
Glow discharge optical emission spectroscopy (GD-OES)
Post-mortem analysis
Lithium plating
SEI growth
Aging mechanism
Si/graphite anodes

A B S T R A C T

Although the loss of Li inventory (LLI) is a common aging mechanism in Li-ion batteries, there are only few methods capable of comprehensive depth profiling within the bulk of the electrode to locate the residual Li. Two post-mortem analytical methods, which can be used to obtain quantified Li depth profiles to depths greater than 10 μm from the electrode surface are neutron depth profiling (NDP) and glow discharge optical emission spectroscopy (GD-OES). In this work, the validation of GD-OES using NDP by examining the Si/graphite anodes of cylindrical 21700 cells is presented. One anode was in a pristine/fresh state, two anodes were aged to the state of health (SOH) 90% and 76% at 45 °C respectively, and suffered from heavy solid electrolyte interphase (SEI) growth, and the fourth anode was aged to SOH 60% at 0 °C and exhibited Li plating. It is demonstrated that Li plating leads to a faster sputter rate of the Li-rich anode surface. An adapted method is introduced to incorporate the changing sputter rate into the depth profile calculation. For the aged anodes, the progressive aging of the anodes leads to a higher amount of irreversibly bound Li on the anode surface.

1. Introduction

Due to the increasing demand for lithium-ion batteries with high-energy density, many efforts have been made in recent decades to develop novel batteries. Thanks to their high theoretical capacity, low cost and abundant natural resources, silicon-based materials have been one of the best candidates to increase the capacity and performance of the battery anodes [1–3]. The Si/graphite composite anodes received much attention, because they combine the high capacity of silicon with the mechanical stability of conventional graphite [4,5]. Up to 4 wt.-% Si is used in anodes of commercial cells [6]. However, during (de-)lithiation, silicon particles undergo significant morphological changes,

* Corresponding author.
E-mail address: Neelima.Paul@frm2.tum.de (N. Paul).
[1] Equal contribution.

which result in an ongoing decomposition of electrolyte at the solid electrolyte interface (SEI) [7]. To better understand the underlying reversible and irreversible degradation processes in Si/graphite electrodes, depth-resolved methods need to be used to obtain information on the decomposition products of the lithium-containing electrolyte across the electrode thickness.

Neutron depth profiling (NDP) is a non-destructive nuclear analytical method, which is used for obtaining quantitative depth specific information of relevant elements in various types of solid materials [8]. Upon irradiation of the material by thermal neutrons, specific isotopes of several light nuclides can emit charged particles after neutron capture: ^{3}He, ^{6}Li, ^{10}B, ^{14}N, ^{17}O, ^{33}S, ^{35}Cl and ^{40}K, including some radioactive nuclides such as: ^{7}Be, ^{22}Na and ^{59}Ni [8]. Because of its high sensitivity for ^{6}Li, NDP has become a well-established technique for the quantification of Li concentration depth profiles in battery electrodes [9]. The following nuclear reaction of a neutron with a ^{6}Li isotope takes place, producing alpha (α) and triton (^{3}H) particles at well-defined energies (Fig. 1a):

$$^{6}\mathrm{Li} + \mathrm{n} \rightarrow \alpha(2055.55\ \mathrm{keV}) + {}^{3}\mathrm{H}\ (2727.92\ \mathrm{keV}) \quad (1)$$

These charged particles gradually lose energy as they penetrate the material before emerging at the sample surface. The energy loss depends on their path length, material composition and the density. The Li concentration depth profile is obtained from the residual energy spectrum of emerged particles [10].

In contrast, glow discharge optical emission spectroscopy (GD-OES) is a spectroscopic method in which a selected area on the sample is sputtered off in a controlled manner and excited in the GD plasma to emit visible light. GD-OES can be used for both qualitative and, with suitable calibration, quantitative elemental analysis of almost all elements in solid samples as a function of depth. Fig. 1b schematically shows the measurement setup of the GD-OES. The sample is placed in electrical contact with the GD-OES cathode opposite to the GD-OES anode. The hollow anode is filled with the discharge gas, e.g. Ar. A high voltage between the sample and the anode releases electrons from the sample, which are accelerated to the anode. Ar atoms are ionized upon collision with the accelerated electrons and subsequently accelerated towards the sample due to their positive charge. Due to the impact of the Ar ions on the sample, the atoms of the sample are sputtered and migrate into the plasma. There they are electrically excited by collisions with electrons and Ar atoms and emit light during de-excitation. The light is focused by a lens onto a concave grating where it is split into individual wavelengths. Photons of element-specific wavelengths are detected with photomultiplier tubes (PMTs) [11].

Both methods have in common that they can perform quantitative depth profiling of Li and therefore can be used to analyze the Li distribution within electrodes from Li-ion batteries. Furthermore, both methods are complementary to each other since they are based on different measurement principles. In Table 1, the main advantages and disadvantages are listed to provide an overview of measuring principles and limitations for each method.

NDP is becoming widely used in Li-ion battery research, where it is applied to complement conventional electrochemical analysis [12–17]. It provides combined information about Li content originating from all lithium-containing compounds in the analyzed electrodes, such as SEI and the lithiated active materials. For example, Wetjen et al. provided insights into depth–resolved information on the reversible and irreversible processes occurring during the formation cycle of Si/graphite electrodes, where both initial SEI formation and ongoing electrolyte decomposition occur uniformly throughout the electrode thickness [12].

Table 1
List of main advantages and disadvantages for the comparison of NDP and GD-OES methods.

NDP	GD-OES
+ non-destructive: counting of particles arising from thermal neutron reaction with ^{6}Li, no external effect of beam/sample interaction	- destructive: effects caused by surface ablation, Ar plasma/sample interaction
- sensitive only to specific isotopes of a few light elements, such as ^{3}He, ^{6}Li, ^{10}B or ^{14}N	+ sensitive to more or less all elements, except F
- neutron facility/proposal needed: longer waiting times	+ laboratory technique: easily available
+ precise Li content determination possible with reference standards	- limited time dependent depth determination
- accessible depth decreases with increasing sample density	+ accessible depth independent on sample density
+ Li content information averaged over the entire sample area can be obtained in the single measurement (sample size up to 20 mm in diameter for battery materials)	- only small sample area is measured (2–4 mm in diameter for battery materials)

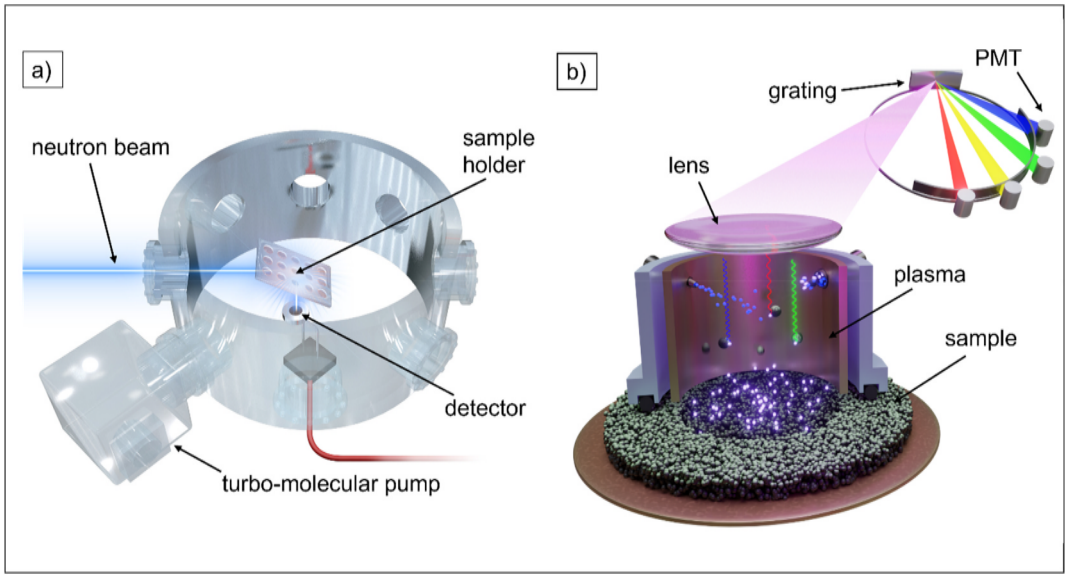

Fig. 1. Schematic comparison of neutron depth profiling (a) and glow discharge optical emission spectroscopy (b) methods: a) The sample is placed in the middle of the vacuum chamber and the detector collects charged particles arising from the ^{6}Li(n,^{4}He)^{3}H nuclear reaction. b) The sample is placed before the plasma chamber and Ar ions sputter off sample atoms. Those atoms are excited in the plasma and emit light, which is recorded with photomultiplier tubes (PMTs).

Moyassari et al. investigated the (de-)intercalation phenomena in Si/graphite porous anodes for the first time using ex-situ NDP during the initial discharge at defined depths of the discharge state [13]. Due to its non-destructive nature, the NDP can also be used for *operando* experiments. Linsenmann et al. developed a novel cell design to obtain information on lithium distribution across the electrode during battery operation [14]. Moreover, Lyons et al. performed *in situ* lithiation of micron-scale Sn foils at a constant potential using a customized Li-ion coin cell design. Lithium diffusion constants were calculated using Fick's 1st and 2nd laws, based on the temporal and spatial changes in Li concentration [15]. In addition, Tomandl et al. successfully investigated migration of Li during the lithiation/delithiation process in ceramic solid electrolytes [16,17].

GD-OES has also been successfully applied to battery electrodes, as well. However, it is a destructive method that creates a crater in the electrode by sputtering with Ar ions. Saito et al. performed the first studies with GD-OES on aged electrodes to investigate the power fading mechanism [18]. Later, Takahara et al. studied the distribution of elements both qualitatively and quantitatively in anodes [19,20]. Takahara et al. demonstrated the application of GD-OES for analysis of SEI and detection of Mn deposition, and studied the effect of small amounts of O_2 or H_2 added to the discharge gas [21,22]. Ghanbari et al. developed a method to detect Li deposition on graphite anodes and studied the inhomogeneous aging of graphite anodes [23,24]. Subsequently, Richter et al. extended the application of GD-OES to state-of-the-art Si/graphite anodes by developing a new calibration for Si content from 0 to 100 wt.-%. The new method was then used to study the aging of Si/graphite anodes and the formation of Si-rich films on the anode surface [25–27]. Recently, Flügel et al. presented a method to determine the minimum amount of elemental Li on Si/graphite anodes [6]. As in Ghanbari et al. [23,24], the method is based on the assumption that Li is bound in the SEI as Li_2O and additionally on the assumption of partially oxidized SiO_x [6]. With the help of all these semi-quantitative GD-OES methods, aging phenomena were detected on the anode surface, i.e. the SEI formation on graphite [23,28] and Si/Graphite anodes [6,26], Li plating on graphite [23,24,29,30] and Si/graphite anodes [6] and Cu re-deposition near the separator [31,32]. These results are consistent with the results obtained by other experimental methods such as cross-sectional *in situ* optical microscopy [33] and Nuclear Magnetic Resonance (NMR) [34], in the case of Li plating with the performed simulations [35]. In some samples, preferential sputtering in GD-OES can occur when different elements in the sample have varying sputter yields. Sputter yield refers to the number of atoms sputtered per incident ion [36]. If the sputter yield is higher for one element compared to another, the element with the higher sputtering yield will be preferentially sputtered, leading to changes in the elemental composition of the surface. So far, preferential sputtering has been studied most extensively in binary samples, in which preferential sputtering leads to a depletion on the surface of the element with the higher sputtering yield [36,37].

Most GD-OES calibration samples were fabricated in-house in a way similar to the fabrication of real electrodes to avoid matrix effects [38]. The calibration samples are graphite coatings with added Li-containing compounds synthesized by aqueous preparation. Due to the reactivity of many Li compounds, calibration samples are limited to 1.34 wt.-% Li, while the Li content in strongly aged anodes exceeds the calibration range.

Other methods commonly used in the elemental analysis of Li-ion batteries include inductively coupled plasma optical emission spectroscopy (ICP-OES), secondary ion mass spectroscopy (SIMS), X-ray photoelectron spectroscopy (XPS) and energy dispersive X-ray spectroscopy (EDX). However, compared to NDP and GD-OES in terms of quantitative analysis of Li depth profile, they have decisive disadvantages. Due to the method of sample collection, ICP-OES cannot provide depth-resolved information [39]. Cross-sections of samples can be obtained using an Ar-ion mill or a focused ion beam, however detection of Li with EDX is not yet possible [40]. XPS and SIMS are surface sensitive methods that can sputter off the samples, but only at a very low sputter rate of 1–10 nm/min [41,42]. In addition, quantification with both methods is very complicated due to the difficult preparation of the reference sample, the surface conditions of the sample and the influence of primary ions.

In this work, we focus on the comparison of the two methods, NDP and GD-OES, for the determination of Li concentration profiles in Si/graphite anodes. Measurements were performed on both fresh and aged Si/graphite anodes to address the GD-OES calibration accuracy issues beyond the calibration range, as well as the influence of their non-destructive (NDP) and destructive (GD-OES) properties on the experimental results.

2. Experimental section

2.1. Electrode characteristics

The studied electrodes are Si/graphite anodes from commercially available 21700 cells with a nominal capacity of 4.85 Ah, a voltage range of 2.5–4.2 V and the maximum charging rate of 0.7C. The thickness of the anode coating is 92 µm with a density of 1.58 g cm ^{3} and porosity is 25.8% in all anodes. The Si amount in the anodes is 3.5 wt.-%. The electrochemical investigations were carried out with Basytec CTS systems and climatic chambers (Vötsch) at ZSW. Aging details of cells, from which anodes A – D were extracted, are summarized in Table 2. The effect of aging on all anodes is schematically shown in Fig. 2. High-temperature aging causes increasing SEI formation for anodes B and C. Low-temperature aging is accompanied by Li plating in case of anode A.

The cells had a voltage of 3.6 V and were at the state of charge (SOC) of 30% when delivered. Formation cycle was performed by the manufacturer. Before cell opening, all cells were discharged at 0.1C at room temperature to 2.5 V (SOC 0%) to extract all anodes in their delithiated state. In this way, all cyclable Li was removed from the anode and the residual Li was expected to be the Li trapped within the SEI, which was also present both at the surface and within the anode bulk due to its porosity. The cell, from which the anode A was extracted, was opened in the glovebox under Ar atmosphere due to the expected Li plating on the anode, while cells, from which anodes B – D were extracted, were opened under ambient conditions. All electrodes were washed three times with dimethyl carbonate (DMC) for 1 min each to remove residual conducting salt.

A 16 mm sample was punched out of each anode from the same central position for NDP examination. GD-OES measurements were performed on electrode areas directly adjacent to the punched-out position. In addition, GD-OES measurements were performed only after the samples arrived at the NDP measurement site to ensure that there were no time dependent effects on the Li concentration measurements.

2.2. Neutron depth profiling

The NDP measurements were performed on the TNDP spectrometer of the NPI CANAM infrastructure at the nuclear research reactor LVR15 in Řež (operated by the Research Center Řež). The TNDP spectrometer is installed on a short vertically curved neutron guide (SwissNeutronics) filtering a beam of the well-thermalized parallel neutrons (Cd ratio ≈

Table 2
Summary of the aging programs of the four cells with the temperature of the climatic chamber, the charge and discharge rate, and the number of cycles until the SOH was reached.

Anode	Temperature	Charging	Discharging	Cycles	SOH
A	0 °C	1C (CCCV)	1C (CC)	34	60%
B	–	–	–	0	100%
C	45 °C	0.5C (CCCV)	0.5C (CC)	180	90%
D	45 °C	0.4C (CCCV)	0.5C (CC)	580	76%

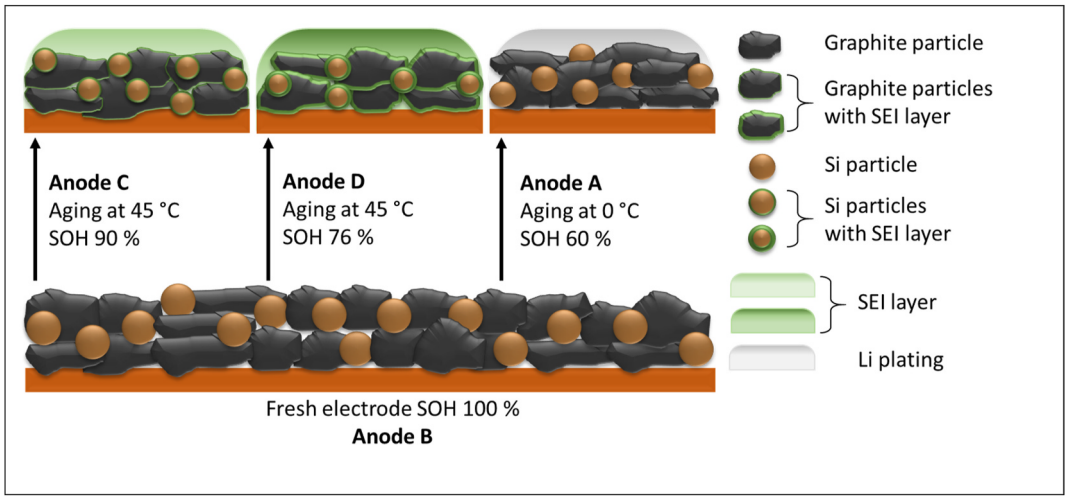

Fig. 2. Schematic summary of four types of analyzed anodes. High-temperature aging causes increasing SEI formation at the electrode shown as a green film. Low-temperature aging is accompanied by Li plating, which is displayed as a grey film on the electrode. (For interpretation of the references to colour in this figure legend, the reader is referred to the Web version of this article.)

10^4) with a neutron thermal flux of 6×10^7 n cm ^{2}s ^{1}. The TNDP spectrometer consists of a multipurpose vacuum chamber and a set of detection systems [43]. During the measurement the neutron beam irradiates the entire sample with an inclination of about 5° to avoid neutron self-shielding. The ^{6}Li(n,^{4}He)^{3}H nuclear reaction (with a high cross-section of 940 b) on the ^{6}Li atoms in the sample is induced. The reaction products (alpha and triton particles) that are isotropically emitted from the reaction sites are then registered by a fully depleted detector (a type of Canberra-Packard, F50143). The detector is positioned coaxially and parallel to the anode surface at a distance of 55 mm. The principle of the method is schematically shown in Fig. 1a.

The energy spectrum of triton (^{3}H) was used to determine the Li depth concentration profiles within the electrodes. Measurement time per sample was 8–35 h, depending on lithium content, in order to obtain sufficient statistics (of a few thousands counts per channel). The measurements of the reference standards with known composition were performed to determine the absolute amount of the Li in the anodes. For the energy calibration, i.e. to convert the channel numbers into an energy scale, a small amount (1.21 ± 0.12 μg/cm^2) of isotopically enriched ^{6}LiF sputtered on a thin Mylar foil was used. The signals of alpha and triton particles are well defined (see Equation (1)) and separated (see Fig. 3a), and therefore both can be used for energy calibration. For the quantity calibration, a round-robin standard with a well-defined ^{10}B content was used. The content of $1.904 \pm 0.015 \times 10^{16}$ ^{10}B/cm^2 was determined after calibration to the SRM2137 standard [44]. For this reference sample, the monitored reaction is ^{10}B(n,^{4}He)^{7}Li and the energy spectra is shown in Fig. 3b. The peak positions are slightly down-shifted compared to the theoretical values due to the implantation of ^{10}B into the Si substrate. However, this does not affect the suitability of the standard for quantitative determination of the Li content in anodes. For the analysis of Li concentration in the anode samples, a natural abundance of ^{6}Li (7.59%) is taken into account [45]. A constant average density is assumed for each anode. The uncertainty in the final Li concentration measured by NDP is estimated to be 10% percent and the depth resolution is 30 nm. The energy loss of tritons in the anodes is calculated using the SRIM (Stopping and Range of Ions in Matter) software, which takes into account different material compositions [46]. The data evaluation was performed using the N4DP software [10,47].

2.3. GD-OES

Glow discharge optical emission spectroscopy (GD-OES) analyses

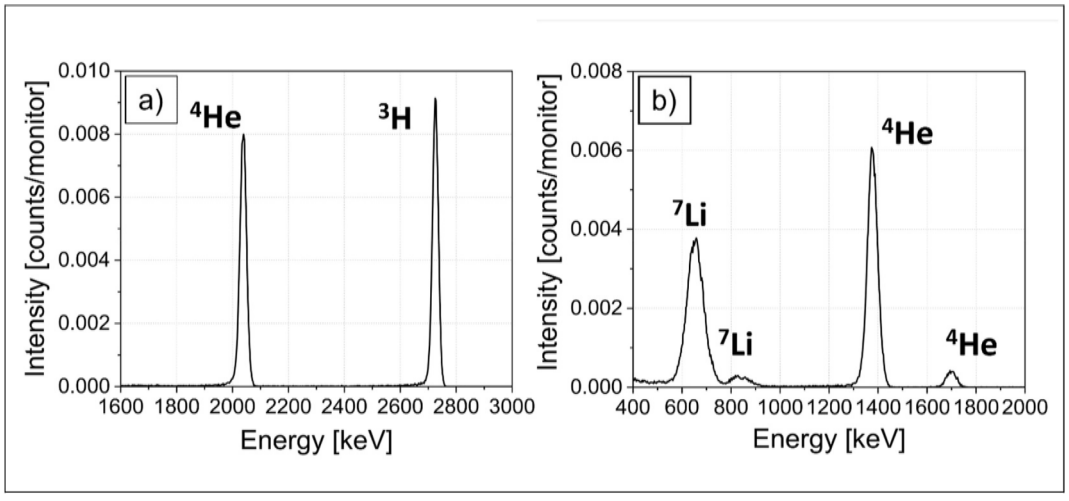

Fig. 3. a) Energy spectrum of ^{6}Li(n,^{4}He)^{3}H for the ^{6}LiF reference sample. b) Energy spectrum of ^{10}B(n,^{4}He)^{7}Li for the boron reference sample. In both cases, signals of ^{4}He and ^{3}H are well separated.

were conducted at ZSW using a GDA750 device (Spectruma) on anode samples. The measurements were performed in radio frequency (RF) mode at a frequency of 2501 Hz, at a discharge voltage of 550 V and at a pressure of 2 hPa. A mixture of 1% H_2 in Ar (both 6.0 purity) was used as a sputter gas. The following element specific emission lines were used for detection: H (121.6 nm), O (130.2 nm), C (156.1 nm), P (178.3 nm), Si (288.1 nm), Li (670.7 nm), Ar (476.5 nm), Ar (696.5 nm), Ar (706.7 nm), Ar (714.7 nm), Ar (727.9 nm). The depth of the crater was determined after a measurement with a Keyence confocal microscope. The Ar lines were detected with a charge-coupled device (CCD) camera while the other lines were detected with photomultiplier tubes (PMTs). The analyzed area has a diameter of 2.5 mm.

2.4. ICP-OES

The inductively coupled plasma optical emission spectroscopy (ICP-OES) measurements were performed at ZSW with an Arcos SOP (Spectro) with Ar 5.0 as carrier gas. For sample collection, the electrode coatings were carefully scraped off from the current collecting foil with a scalpel.

2.5. SEM

Scanning electron microscopy (SEM) of electrodes was carried out at ZSW with a secondary electron (SE) detector at 5 kV using a high-performance LEO 1530 VP (Zeiss) microscope equipped with a Gemini thermal field emission column. EDX mappings were recorded at an acceleration voltage of 10 kV. Cross-sections of anodes were generated with a Hitachi IM4000Plus broad-beam Ar ion milling system, using an ion beam voltage of 5 kV. During sample preparation for SEM top view and cross-section, the samples were exposed to air.

3. Results and discussion

The cell samples chosen were specifically selected to study the effects of anode aging. One cell was disassembled at 100% SOH to determine the Li distribution of a fresh anode. Based on the Li distribution in the unaged state, the changes in Li distribution were investigated after different aging mechanisms. At elevated temperatures, the solid-electrolyte interphase (SEI) decomposes, dissolves or undergoes structural changes, resulting in the reformation of the SEI and a continuous increase in SEI thickness [48]. This phenomenon occurs ubiquitously on the active material within the anode, resulting in an expected homogeneous increase in Li distribution. The SEI accumulates over a significant number of cycles, coinciding with a gradual depletion of the electrolyte. Consequently, as the electrodes dry out, there is a rapid decline in cell capacity. This is in contrast to aging at lower temperatures, at which the Li intercalation is kinetically slowed down. At high charge rates and lower temperatures, the anode potential drops below 0 V vs. Li/Li^+, thermodynamically favoring the deposition of elemental Li [49]. This results in a non-uniform lithium distribution due to the deposition of lithium on the anode surface. Deposited lithium is susceptible to reacting with the electrolyte or may experience electrical disconnection, leading to a decrease in lithium inventory and consequently a significant loss of capacity [50]. These two aging mechanisms were selected in order to be able to compare GD-OES and NDP for the most different anode aging phenomena.

3.1. Detection of Li plating

The comparison between NDP and GD-OES is intended to demonstrate the reliability and accuracy of GD-OES depth profiles. The challenge is the lack of suitable calibration samples with a high Li content. Many aged anode samples have an average Li content or show Li plating, which is beyond the calibration range of GD-OES.

Fig. 4 shows the Li depth profiles of anode A in the range of 0–16 µm

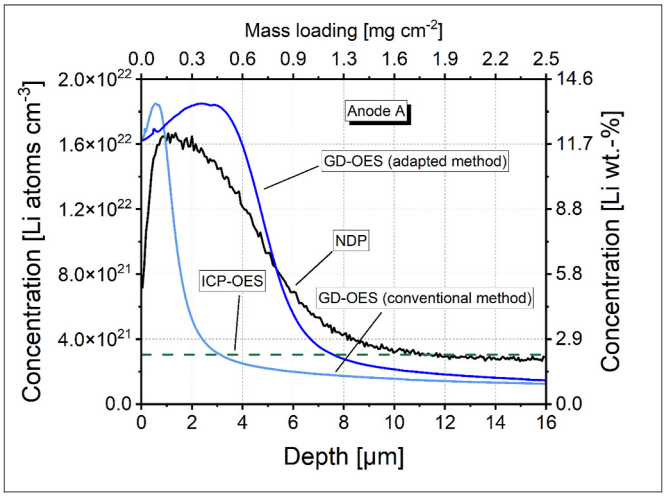

Fig. 4. Comparison of the NDP depth profile (black) with the GD-OES depth profiles of Li using both the conventional method (light blue) and the adapted method (dark blue) for depth calculation for anode A. (For interpretation of the references to colour in this figure legend, the reader is referred to the Web version of this article.)

measured by NDP (black) and GD-OES (light blue and dark blue), starting at 0 µm at the electrode/separator interface. Additionally, the green line indicates the average (i.e. depth independent) Li concentration of the electrode determined by ICP-OES. The graph shows two GD-OES depth profiles whose depth calculation was performed according to the so called "conventional method" (light blue) and with the so called "adapted method" (dark blue) described later.

ICP-OES analysis resulted in an average total Li content of 2.22 ± 0.09 wt.-% corresponding to $3.04 \times 10^{21} \pm 0.12 \times 10^{21}$ Li atoms cm^{-3} from the surface to the current collector. Since this sample was aged at low temperatures, a very inhomogeneous Li distribution can be expected along the depth of the anode. The NDP examination reveals a high Li value in the upper 8 µm from the anode surface, which decreases towards the bulk. The maximum content of the Li plating measured by NDP is 1.67×10^{22} Li atoms cm^{-3} or 12.2 wt.-% with a maximum depth of the Li plating of 6–8 µm. At the depth of 8–16 µm from the surface, the NDP depth profile shows a much lower Li content and is approaching the average value estimated by the ICP-OES in the bulk. Due to the very high Li content at the surface, the Li concentration is slightly below the average bulk Li concentration below a depth of 12 µm. The surface peak in the NDP measurements is in qualitative agreement with previous GD-OES measurements [6,19,20,23–26] and simulations [35] of anodes with Li deposition.

The GD-OES depth profile shows a similar pattern of Li distribution in the electrode. Near the surface the maximum concentration of 13.7 wt.-% (1.8×10^{22} Li atoms cm^{-3}) is found and it decreases rapidly towards the bulk. However, the depth profile of the deposited Li evaluated by the conventional method (light-blue curve in Fig. 4) significantly differs from the NDP measurement. Although the thickness of the Li plating layer is approximately 8 µm with NDP, only approximately 2 µm was determined with GD-OES with the conventional method.

During cycling at low temperatures, the intercalation kinetics decrease and the over-potentials increase. At anode potentials below 0 V vs. Li/Li^+ the deposition of metallic Li is favored over the intercalation of Li into the anode. Recently, we have shown that the addition of Si, which allows the reduction of the anode thickness at constant areal capacity, decreases the risk of Li plating. Anodes containing Si only showed Li plating at higher C-rates than graphite anodes with the same areal capacity. The amount of metallic Li found on this anode might have been reduced by the addition of Si as anode active material [51].

During GD-OES measurement, the mass fraction of each element

versus sputter time is recorded. The conventional method of calculating the sputter depth from the sputter time is based on the assumption that the sputter rate is constant. The sputter rate should be indeed constant if the elements present in the sample are homogeneously distributed and no preferential sputtering is occurring. However, because the sputter rate of the Li-rich layer in the anode is much higher than that of the graphite, the GD-OES analysis with the conventional method gives a thickness of only approximately 2 µm, while the actual thickness is about 8 µm.

In order to confirm the thickness of the Li plating layer determined by NDP using another method, we acquired SEM and EDX images of the cross-section of anode A. Fig. 5a shows the EDX mapping of the elements C, O and Si at the cross-section of anode A. Due to exposition to air during the sample preparation, the deposited Li could be oxidized, so we can get a hint on Li deposition through the O signal. The image shows that the Li deposition on the anode surface is most likely 6–10 µm thick. This observation is consistent with the NDP depth profile of anode A, in which the Li content drops sharply after 6 µm and the bulk concentration of Li is reached after about 10 µm. Due to the short aging of 34 cycles, no noticeable amount of SEI is seen around the Si particles in the bulk, confirming there is only low Li content in the bulk.

3.2. Further development of GD-OES depth profiling method

The use of complementary methods such as NDP and SEM of cross-sectioned anodes is a complex and expensive analytical approach and it is not available for every GD-OES measurement. Therefore, we were looking for a way to calculate the depth parameter more correctly using the data provided by GD-OES, which takes into account the different sputter rates.

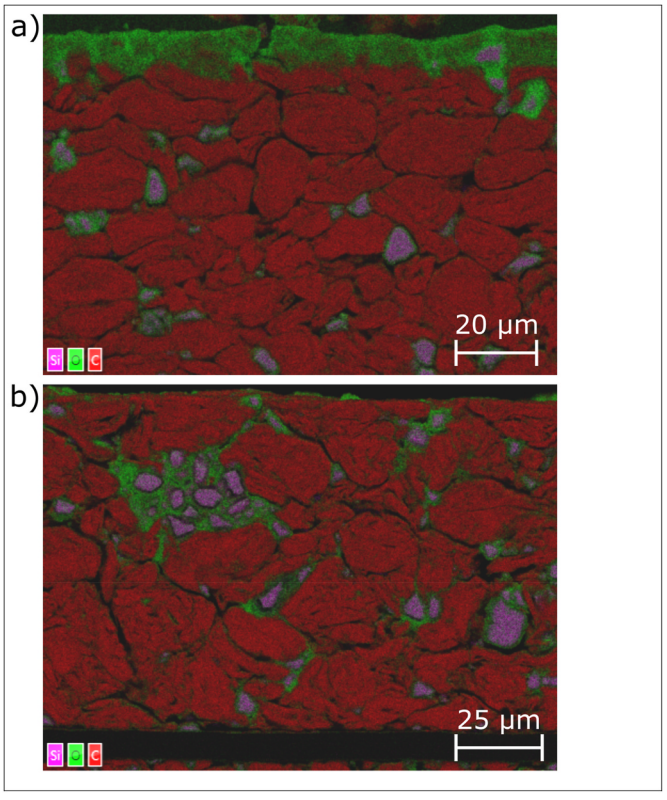

Fig. 5. Cross-sections of anode A (a) and anode D (b) recorded with EDX elemental mapping showing Si (magenta), O (green) and C (red). a) Due to the sample preparation, the Li deposition is oxidized, therefore Li deposition is indicated by the O signal. b) The Si particles exhibit distinctive SEI films due to aging. (For interpretation of the references to colour in this figure legend, the reader is referred to the Web version of this article.)

Here, we present a new adapted method of converting the sputter time into the respective sputter depth based on the intensity of Ar lines, which are simultaneously recorded during measurement with CCD cameras. Ar is used as a sputtering gas and plasma component in every measurement, and it emits light during the measurement. Fig. 6 shows the intensity of the Ar lines at 714.704 nm (red, "Ar715") and 727.294 nm (blue, "Ar727") as well as the Li intensity of anode A, which has Li plating, and anode B, the pristine/fresh anode, which is used as a reference here.

It is obvious that the Ar727, Ar715, and Li intensities behave similarly for both anodes A and B, respectively. Anode B shows a nearly uniform Ar intensity and a constant sputter rate (Fig. 6c). However, the Li-rich surface of anode A causes an increase in Ar intensity during the sputtering of this layer (Fig. 6a). After the Li has been sputtered off from the anode surface, recognizable by the decreasing Li intensity, the Ar intensity also decreases and reaches a stable value, which it maintains for the rest of the measurement. During measurements, sample atoms can be excited by collisions with Ar atoms in the plasma. In the same way, Ar atoms can also be excited by collisions with sample atoms [52]. Due to the increase of the sample concentration in the plasma, caused by the high sputter rate, the probability of collisions increases. In addition, the current increases during the high sputter rates, which also increases the excitation by elastic and inelastic collisions with electrons [53]. Consequently, there is a correlation between the sputter rate and the Ar intensity [54,55].

Parker et al. already found that the intensity of certain Ar lines shows a similar behavior as the sputter rate [54]. We assumed that the intensity of some Ar lines is proportional to the sputter rate for the measurement of porous electrodes. Therefore, the depth d at a point in time can be calculated by the term given in equation (2):

$$d = D\frac{\int_0^z I_{Ar}(t)dt}{\int_0^t I_{Ar}(t)dt} \tag{2}$$

where D is the total depth at the end of the measurement, z is the time, t is the total measurement duration, and I_{Ar} is the intensity of the Ar line. An example of the depth calculation is provided in the Supplementary Information (Fig. S1).

In Fig. 6c, the depth parameter of the anodes A and B is calculated using equation (2) and is plotted as a function of time. It can be seen that for anode A, which has Li plating on the surface, a sputter depth of ~6 µm is achieved in the first 200 s. From 200 s onwards, equilibrium is reached and the increase in depth with time is approximately linear, corresponding to a nearly constant sputter rate. Equilibrium is reached when the excess of Li due to Li plating is removed, and Li, which is still intercalated or present in the SEI can only be removed after being exposed to sputtering ions after the covering graphite is removed. In contrast, anode B shows a uniform sputter rate from the beginning with a crater depth of 2.5 µm achieved after 200 s.

Using the equation presented in equation (2), the depth of anode A is recalculated from the measurement time in Fig. 4 (dark blue curve). The adapted depth calculation provides a significantly improved agreement between the NDP and GD-OES measurements. The maximum Li amount is not affected by the recalculation, only the width of the Li plating peak is increased. This changes the amount of Li plating between 0 and 10 µm from 4.48×10^{22} Li atoms cm ^{3} to $9.99 \times 10^{22} \pm 0.03 \times 10^{22}$ Li atoms cm ^{3} and is very similar to the NDP result of 9.54×10^{22} Li atoms cm ^{3}. The deviation results from the use of the different Ar lines to calculate the depth. Since the results are very similar, any of the Ar lines listed (AR727 for dark blue curve in Fig. 4) can be used for the depth calculation. The amount of detected Li by GD-OES from the surface to the current collector foil is 2.2 wt.-%, compared to 2.22 wt.-% measured by ICP-OES. The reason that the Li content in the 8–16 µm range with GD-OES is below the concentration determined with NDP could be a measurement artifact of the preferential sputtering, which will be described later.

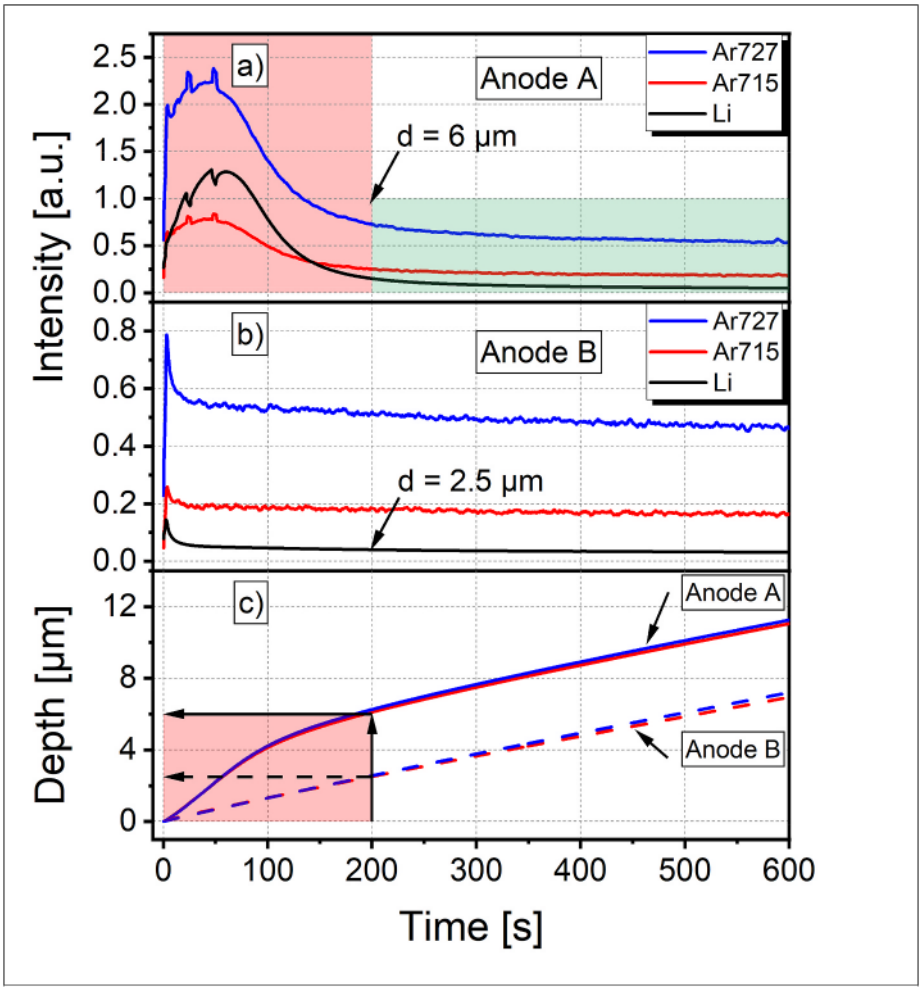

Fig. 6. Plot of Ar and Li intensity versus time for a) anode A and b) anode B, showing that Ar intensities behave similarly to the sputter rate; c) Sputter depth versus sputter time, demonstrating that in anode A a higher sputter depth is reached within the first 200 s before the sample sputter becomes constant.

We note that the previous results with GD-OES methods to quantify Li plating semi-quantitatively on graphite [23,24] and Si/graphite anodes [6] are still valid using the adapted depth calculation. Based on the detected amount of O and Si, these methods determine the minimum amount of elemental Li. However, with the improved depth calculation as presented here, the depth distribution is represented more accurately.

3.3. Detection of SEI growth

Fig. 7a–c shows the NDP and GD-OES depth profiles of anodes B, C, and D. Anode B is the anode of a pristine/fresh cell (100% SOH), while anodes C and D were aged at 45 °C until 90% and 76% SOH, respectively. All cells were fully discharged to the end-of-charge voltage before opening. Therefore, the detected Li corresponds to irreversibly lost Li inventory and residual intercalated Li. In addition to the NDP depth profile (black) and the two GD-OES depth profiles (blue), the average Li content determined by ICP-OES is also plotted as a dashed green line in the graphs. Due to the partial overlapping of alpha and triton particle energies, caused by higher electrode thickness, only the range 0–16 µm is examined using NDP. The ICP-OES analysis results in a Li content of the three samples: 1.56 wt.-% (anode B), 2.16 wt.-% (anode C) and 2.61 wt.-% (anode D). As can be seen, all contents are above the range of 0–1.34 wt.-% Li in the calibration samples of GD-OES. Due to the high irreversible loss of Li to the SEI during formation cycles, particularly due to presence of Si, the percentage of Li in a pristine/fresh, discharged cell is already above 1.35 wt.-%.

All NDP depth profiles show a Li peak on the anode surface and the Li content in the bulk continues to increase with aging. The increased Li content with aging is consistent with Waldmann et al., Iturrondobeitia et al. and Wetjen et al. [28,30,56]. This observation can be attributed to the irreversible binding of Li in the SEI and within the films around the active material particles, especially the Si particles [57,58]. Furthermore, it can be seen that the Li depth profile for anode B is very uniform, while for anode C it exhibits a slight decrease towards the anode bulk, and for anode D, on the contrary a slight increase starting at around 6 µm. Additionally, the Li concentration in the upper 16 µm of the anode are higher than the average Li-level of the electrode, which suggests that the Li gradient may continue even further towards the current collector.

Fig. 5b shows the EDX element mapping of the cross-section of anode D in which O is shown in green, Si in magenta, and C in red. Because the sample was in contact with atmospheric O during the preparation, a reaction with O_2 cannot be excluded. It can be very clearly seen that a thick layer of SEI is formed around the Si particles. The very thick SEI suggests that high amounts of Li are irreversibly bound in the anode, which has been reported in the literature [6,59,60]. Furthermore, it appears that the SEI layer of the particles near the anode surface is thicker than the SEI of the Si particles near the Cu collecting foil, as was already observed by Richter et al. [25,26].

GD-OES measurements are possible through the entire electrode coating up to the Cu current collector foil. Thus, the elemental distribution in the electrode can be measured, and by integration [23], the total amount of an element can be determined. Li concentrations

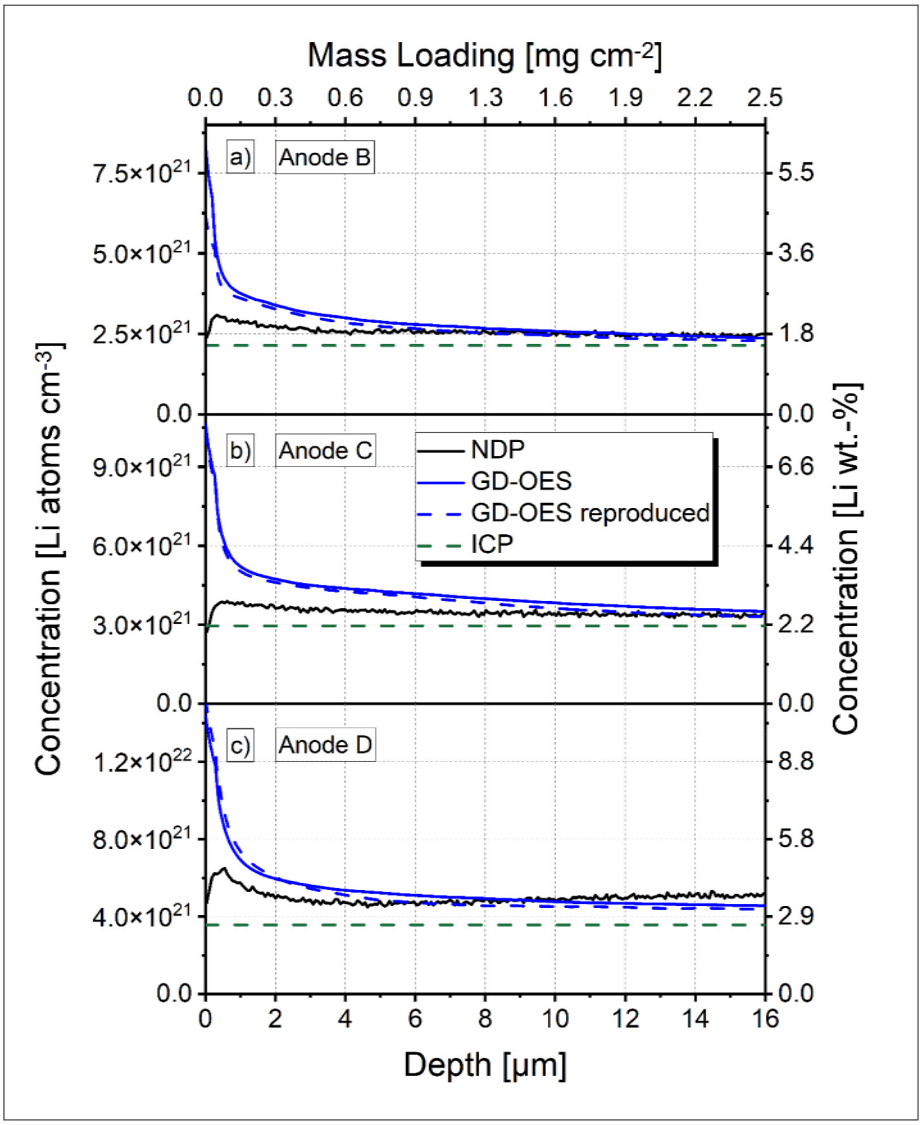

Fig. 7. NDP (black) and GD-OES (blue) depth profiles of anodes B, C and D at a depth of 0 µm (surface) to 16 µm; ICP-OES measurements (green) show the average Li content in the sample. (For interpretation of the references to colour in this figure legend, the reader is referred to the Web version of this article.)

obtained with GD-OES in anodes B, C and D are 1.58 ± 0.08 wt.-%, 2.21 ± 0.18 wt.-% and 2.76 ± 0.22 wt.-%, respectively. For low Li values such as in anode B, the Li concentration determined with GD-OES is close to that measured with ICP-OES. While the difference to the ICP-OES Li concentration increases with aging, the ICP-OES result is within the error range of the GD-OES measurement. Therefore, GD-OES calibration for Li has been shown to provide reliable results even outside its calibration range. For GD-OES measurements of aged anodes, which do not have Li deposition on the surface, the adapted method was not applied. Since Li is distributed in the anode and does not form a separate Li-rich layer on the anode surface, the sputter rate is the same as the carbon sputter rate and therefore is constant throughout the electrode.

In comparison with the NDP depth profiles, it can be seen that the Li peak on the anode surface is also evident in the GD-OES depth profiles, where the peak is more pronounced. In addition, the Li content at the electrode surface measured with GD-OES increases due to progressed aging. From the surface of the anode towards the electrode bulk, a slight difference in the Li concentration is observed in the profiles of both measurement methods. The GD-OES measurement yields higher concentrations in each measurement. The decrease in Li concentration from the surface towards the bulk, detected by NDP, is also observed by GD-OES. Since the decrease in the GD-OES measurements is steeper, the GD-OES and NDP profiling values converge to be equal from 12 µm depth onwards. The Li gradient is caused by the inhomogeneous distribution of Li in the anodes, with more Li found in the SEI near the anode surface. This result is consistent with the findings of Takahara et al., who observed inhomogeneous Li depth profiles in degraded anodes [22].

As discussed, GD-OES and NDP Li depth profiles show consistent results with regard to the Li prominent peak at the anode surface, a higher than average Li content (measured by ICP-OES) on the anode surface, increased Li content due to the aging mechanism, and the Li gradient from the surface toward the bulk.

However, the different Li concentration in the uppermost 10 µm of the anode surface measured with GD-OES and NDP is most likely caused by preferential sputtering [37], which is described and discussed below.

It is evident from Fig. 7a–c that GD-OES depth profiles reveal a higher Li concentration at the surface than NDP measurements. The difference between the NDP and GD-OES concentrations is 1×10^{21} Li atoms cm ^{3} at a depth of 0.5 µm for anode B, however, they both methods measure the same Li concentration at a depth of 6 µm. For anode C, the difference in the Li concentration between GD-OES and NDP is 2×10^{21} Li atoms cm ^{3} at a depth of 0.5 µm and both methods measure the same Li concentration only from a depth of 12 µm. The difference is most serious in anode D, where it is 3×10^{21} Li atoms cm ^{3}

at the anode surface, although even higher Li value can be observed for NDP from a depth of 10 µm.

During preferential sputtering, an element with a high sputter rate is sputtered faster than other elements with a lower sputter rate [37]. The occurrence of this phenomenon is known, for example, in metal oxides, where O is removed faster than the metal atom [61]. This leads to a relative enrichment of the element with a lower sputter rate at the anode surface and additional O can only be sputtered off when the metal atoms are sputtered off beforehand.

In contrast to metal oxides, Li-ion anodes consist of mainly graphite particles, which have a very low sputter rate, and which are covered with Li containing SEI. We found out in section 3.1, that Li has a much higher sputter rate than graphite. However, the anodes B, C and D do not consist of Li-rich layer on the anode surface, but Li is distributed much more uniformly in the anode.

The resulting sputtering process is schematically shown in Fig. 8. When the sputtering process starts, the SEI covering the anode is sputtered off. As the SEI has a high Li content, it results in the Li peak that is observed with GD-OES. Moreover, NDP and SEM confirm the presence of a Li-rich SEI, which is most pronounced at the surface. As the sputtering process proceeds, the anode surface is depleted of the SEI, which means that the SEI located between the graphite particles of the top layer can easily be sputtered off. As illustrated in Fig. 8, compared to the real composition in the anode, the plasma composition exhibits a higher Li content. This is most likely the reason for an increased Li concentration in the GD-OES depth profiles. In addition to the decreasing Li content towards the electrode bulk, we observe a Li depletion on the anode surface, resulting in a steeper Li gradient in the GD-OES depth profiles. Further Li can only be sputtered off when graphite is ablated to expose the SEI layer of the second graphite layer. This equilibrium is the reason why the Li concentration of GD-OES and NDP are the same below a depth of 12 µm as this is approximately the thickness of one graphite particle. The effect of preferential sputtering is more evident in highly aged cells with increasing SEI thickness.

Although we observe preferential sputtering for aged Si/graphite anodes, its consequence for the quality of the results is limited. The phenomenon of preferential sputtering does not lead to increased Li values, as evidenced by the comparison of GD-OES with ICP-OES. The trend of the Li distribution is similar for both methods GD-OES and NDP.

4. Conclusion

In this work, we successfully applied both methods, NDP and GD-OES, to measure depth profiles of Li in Si/graphite anodes after post-mortem analysis of Li-ion batteries. The comparison of the two complementary techniques has served to further improve the GD-OES method for depth profiling of Li in electrodes.

Due to the limited availability of suitable calibration samples with sufficiently high Li mass fraction, validation of the GD-OES method outside the calibration range is necessary. In this work, it is shown that by comparison with ICP-OES that GD-OES, we can reliably determine the Li content by data integration. In addition, by comparison with NDP, we have shown that the distribution of Li as a function of depth can be determined by GD-OES with sufficient accuracy. While the detected concentrations of most elements measured with GD-OES in LIB anodes are within the concentration range of the respective element, the concentrations measured for Li are outside the Li calibration range, as only calibration samples up to 1.34 wt.-% were prepared due to the high reactivity of many Li compounds. Even though the results of the comparison showed that the Li concentration could also be reliably measured outside the calibration range, an option for producing calibration samples with higher Li content is to use lithium compounds with atoms that are not present in LIB or are present in very low concentrations, such as Li chloride or Li nitrate.

We succeed in demonstrating the faster sputtering of Li plating from the anode and in establishing an equation to perform the depth calculation more accurately. The conventional method was based on the assumption of a homogeneous sputter rate, which led to uncertainty regarding the width of the Li plating peak in the GD-OES depth profiles. This bias can be eliminated using the adapted method developed in the present work, since in the case of Li-ion anodes it has been shown that the sputter rate can be approximately modelled by the Ar intensity.

Furthermore, we observe that the preferential sputtering can occur on the anode surface. This phenomenon is caused by the higher sputter rate of Li, as it is mainly present in the Li plating layer or in the SEI near the surface. Although this effect occurred and was observable through the differences in the GD-OES depth profiles from the NDP depth profiles, it did not affect the main results. The NDP measurements showed that the Li content has the highest value at the surface and decreases slightly with depth. This finding is consistent with previous GD-OES and

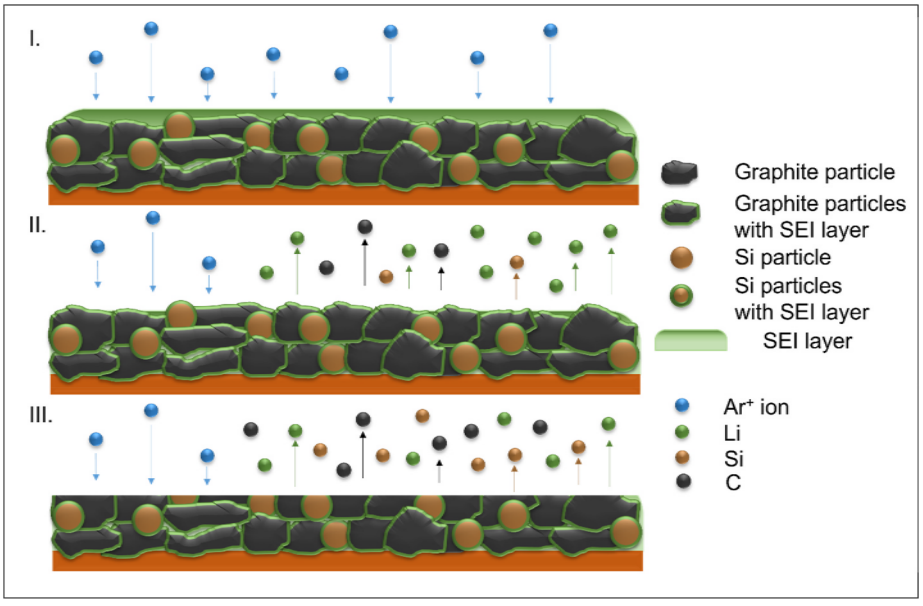

Fig. 8. Schematic explanation of the preferential sputtering phenomenon. I. The surface of the anode sample is bombarded by Ar ions. II. In a Li-containing SEI top layer, Li atoms are preferentially sputtered off. III. In the bulk, equilibrium is established and Li, C and Si atoms are sputtered at the same rates.

NDP results.

CRediT authorship contribution statement

Ivana Pivarníková: Formal analysis, Methodology, Writing – original draft, Writing – review & editing, Investigation. **Marius Flügel:** Formal analysis, Investigation, Methodology, Writing – original draft, Writing – review & editing. **Neelima Paul:** Conceptualization, Formal analysis, Investigation, Methodology, Supervision, Writing – original draft, Writing – review & editing. **Antonino Cannavo:** Methodology, Writing – review & editing. **Giovanni Ceccio:** Methodology, Writing – review & editing. **Jiří Vacík:** Methodology, Resources, Writing – review & editing. **Peter Müller-Buschbaum:** Funding acquisition, Supervision, Writing – review & editing. **Margret Wohlfahrt-Mehrens:** Funding acquisition, Supervision, Writing – review & editing. **Ralph Gilles:** Funding acquisition, Supervision, Project administration, Writing – review & editing. **Thomas Waldmann:** Conceptualization, Funding acquisition, Project administration, Resources, Supervision, Writing – review & editing.

Declaration of competing interest

The authors declare that they have no known competing financial interests or personal relationships that could have appeared to influence the work reported in this paper.

Data availability

Data will be made available on request.

Acknowledgement

I.P. and M.F. contributed equally to this work. The authors acknowledge the German Federal Ministry of Education and Research (BMBF) for funding the project CharLiSiKo (03XP0333A) within the AQua cluster and the project ExZellTUM III (03XP0255) within the ExcellBattMat cluster. Furthermore, the authors thank Reiner Müller (MLZ) for the creation of Fig. 1a, Emanuele Marini (ZSW) for the creation of Fig. 1b, Claudia Pfeifer (ZSW) for EDX measurements and Gisela Arnold (ZSW) for ICP-OES measurements. The NDP measurements were carried out at the NPI and RC infrastructures 'CANAM' and 'Reactors LVR-15 and LR-0' in Řež (CR) supported by Ministry of Education, Youth and Sports of the Czech Republic (projects No. LM2015056 and LM2015074).

References

[1] X.X. Zuo, J. Zhu, P. Muller-Buschbaum, Y.J. Cheng, Nano Energy 31 (2017) 113–143, https://doi.org/10.1016/j.nanoen.2016.11.013.
[2] J.R. Szczech, S. Jin, Energy Environ. Sci. 4 (2011) 56–72, https://doi.org/10.1039/C0EE00281J.
[3] G.G. Eshetu, H. Zhang, X. Judez, H. Adenusi, M. Armand, S. Passerini, E. Figgemeier, Nat. Commun. 12 (2021) 5459, https://doi.org/10.1038/s41467-021-25334-8.
[4] J. Asenbauer, T. Eisenmann, M. Kuenzel, A. Kazzazi, Z. Chen, D. Bresser, Sustain. Energy Fuels 4 (2020) 5387–5416, https://doi.org/10.1039/D0SE00175A.
[5] P. Li, H. Kim, S.-T. Myung, Y.-K. Sun, Energy Storage Mater. 35 (2021) 550–576, https://doi.org/10.1016/j.ensm.2020.11.028.
[6] M. Flügel, K. Richter, M. Wohlfahrt-Mehrens, T. Waldmann, J. Electrochem. Soc. 169 (2022) 050533, https://doi.org/10.1149/1945-7111/ac70af.
[7] J. Kim, O.B. Chae, B.L. Lucht, J. Electrochem. Soc. 168 (2021) 030521, https://doi.org/10.1149/1945-7111/abe984.
[8] R.G. Downing, G.P. Lamaze, J.K. Langland, S.T. Hwang, J. Res. Natl. Inst. Stand. Technol. 98 (1993) 109–126, https://doi.org/10.6028/jres.098.008.
[9] S. Whitney, S.R. Biegalski, Y.H. Huang, J.B. Goodenough, J. Electrochem. Soc. 156 (2009) A886–A890, https://doi.org/10.1149/1.3216033.
[10] M. Trunk, M. Wetjen, L. Werner, R. Gernhauser, B. Markisch, Z. Revay, H. A. Gasteiger, R. Gilles, Mater. Char. 146 (2018) 127–134, https://doi.org/10.1016/j.matchar.2018.09.030.
[11] R.K. Marcus, J.A. Broekaert, Glow Discharge Plasmas in Analytical Spectroscopy, Wiley Online Library, 2003, https://doi.org/10.1002/0470857854.
[12] M. Wetjen, M. Trunk, L. Werner, H.A. Gasteiger, R. Gernhauser, R. Gilles, B. Markisch, Z. Revay, J. Electrochem. Soc. 166 (2019) A1408–A1411, https://doi.org/10.1149/2.0581908jes.
[13] E. Moyassari, L. Streck, N. Paul, M. Trunk, R. Neagu, C.-C. Chang, S.-C. Hou, B. Märkisch, R. Gilles, A. Jossen, J. Electrochem. Soc. 168 (2021) 020519, https://doi.org/10.1149/1945-7111/ac4545.
[14] F. Linsenmann, M. Trunk, P. Rapp, L. Werner, R. Gernhäuser, R. Gilles, B. Märkisch, Z. Revay, H. Gasteiger, J. Electrochem. Soc. 167 (2020), https://doi.org/10.1149/1945-7111/ab9b20.
[15] D.J. Lyons, J.L. Weaver, A.C. Co, J. Mater. Chem. A 10 (2022) 2336–2351, https://doi.org/10.1039/D1TA09639G.
[16] I. Tomandl, J. Vacik, T. Kobayashi, Y. Mora Sierra, V. Hnatowicz, V. Lavreniev, P. Horak, G. Ceccio, A. Cannavo, M. Baba, R. Ye, Radiat. Eff. Defect Solid 175 (2020) 394–405, https://doi.org/10.1080/10420150.2019.1701471.
[17] I. Tomandl, T. Kobayashi, A. Cannavó, J. Vacík, G. Ceccio, T. Sassa, V. Hnatowicz, J. Power Sources 542 (2022) 231719, https://doi.org/10.1016/j.jpowsour.2022.231719.
[18] Y. Saito, M.K. Rahman, J. Power Sources 174 (2007) 877–882, https://doi.org/10.1016/j.jpowsour.2007.06.223.
[19] H. Takahara, H. Miyauchi, M. Tabuchi, T. Nakamura, J. Electrochem. Soc. 160 (2012) A272, https://doi.org/10.1149/2.061302jes.
[20] H. Takahara, M. Shikano, H. Kobayashi, J. Power Sources 244 (2013) 252–258, https://doi.org/10.1016/j.jpowsour.2013.01.109.
[21] H. Takahara, Y. Kobayashi, K. Shono, H. Kobayashi, M. Shikano, T. Nakamura, J. Electrochem. Soc. 161 (2014) A1716, https://doi.org/10.1149/2.1011410jes.
[22] H. Takahara, A. Kojyo, K. Kodama, T. Nakamura, K. Shono, Y. Kobayashi, M. Shikano, H. Kobayashi, J. Anal. Atomic Spectrom. 29 (2014) 95–104, https://doi.org/10.1039/c3ja50183c.
[23] N. Ghanbari, T. Waldmann, M. Kasper, P. Axmann, M. Wohlfahrt-Mehrens, J. Phys. Chem. C 120 (2016) 22225–22234, https://doi.org/10.1021/acs.jpcc.6b07117.
[24] N. Ghanbari, T. Waldmann, M. Kasper, P. Axmann, M. Wohlfahrt-Mehrens, ECS Electrochem. Lett. 4 (2015) A100–A102, https://doi.org/10.1149/2.0041509eel.
[25] K. Richter, T. Waldmann, M. Memm, M. Kasper, M. Wohlfahrt-Mehrens, J. Electrochem. Soc. 165 (2018) A3602, https://doi.org/10.1149/2.0071816jes.
[26] K. Richter, T. Waldmann, M. Kasper, C. Pfeifer, M. Memm, P. Axmann, M. Wohlfahrt-Mehrens, J. Phys. Chem. C 123 (2019) 18795–18803, https://doi.org/10.1021/acs.jpcc.9b03873.
[27] K. Richter, T. Waldmann, N. Paul, N. Jobst, R.G. Scurtu, M. Hofmann, R. Gilles, M. Wohlfahrt-Mehrens, ChemSusChem 13 (2020) 529–538, https://doi.org/10.1002/cssc.201903139.
[28] T. Waldmann, N. Ghanbari, M. Kasper, M. Wohlfahrt-Mehrens, J. Electrochem. Soc. 162 (2015) A1500–A1505, https://doi.org/10.1149/2.0411508jes.
[29] T. Waldmann, J.B. Quinn, K. Richter, M. Kasper, A. Tost, A. Klein, M. Wohlfahrt-Mehrens, J. Electrochem. Soc. 164 (2017) A3154, https://doi.org/10.1149/2.0961713jes.
[30] A. Iturrondobeitia, F. Aguesse, S. Genies, T. Waldmann, M. Kasper, N. Ghanbari, M. Wohlfahrt-Mehrens, E. Bekaert, J. Phys. Chem. C 121 (2017) 21865–21876, https://doi.org/10.1021/acs.jpcc.7b05416.
[31] M. Flügel, M. Kasper, C. Pfeifer, M. Wohlfahrt-Mehrens, T. Waldmann, J. Electrochem. Soc. 168 (2021) 020506, https://doi.org/10.1149/1945-7111/abdc5f.
[32] M. Flügel, T. Waldmann, M. Kasper, M. Wohlfahrt-Mehrens, ChemPhysChem 21 (2020) 2047–2050, https://doi.org/10.1002/cphc.202000333.
[33] C. Hogrefe, T. Waldmann, M. Hölzle, M. Wohlfahrt-Mehrens, J. Power Sources 556 (2023) 232391, https://doi.org/10.1016/j.jpowsour.2022.232391.
[34] B.P. Matadi, S. Geniès, A. Delaille, T. Waldmann, M. Kasper, M. Wohlfahrt-Mehrens, F. Aguesse, E. Bekaert, I. Jiménez-Gordon, L. Daniel, J. Electrochem. Soc. 164 (2017) A1089, https://doi.org/10.1149/2.0631706jes.
[35] S. Hein, A. Latz, Electrochim. Acta 201 (2016) 354–365, https://doi.org/10.1016/j.electacta.2016.01.220.
[36] R. Shimizu, Nucl. Instrum. Methods Phys. Res. Sect. B Beam Interact. Mater. Atoms 18 (1986) 486–495, https://doi.org/10.1016/S0168-583X(86)80074-X.
[37] H. Werner, N. Warmoltz, Surf. Sci. 57 (1976) 706–714, https://doi.org/10.1016/0039-6028(76)90356-3.
[38] R. Payling, T. Nelis, R.F. Browner, J.M. Chalmers, M.S. Cresser, J.J. Monaghan, A. Sanz Medel, R.D. Snook, F. Adams, M.J. Adams, B. Chase, B. Hoving, Glow Discharge Optical Emission Spectroscopy: A Practical Guide, The Royal Society of Chemistry, 2003, https://doi.org/10.1039/9781847550989.
[39] B. Vortmann-Westhoven, M. Winter, S. Nowak, J. Power Sources 346 (2017) 63–70, https://doi.org/10.1016/j.jpowsour.2017.02.028.
[40] I.D. Campbell, M. Marzook, M. Marinescu, G.J. Offer, J. Electrochem. Soc. 166 (2019) A725, https://doi.org/10.1149/2.0821904jes.
[41] Y. Feng, B.M. Koo, A. Seyeux, J. Swiatowska, C. Henry de Villeneuve, M. Rosso, F. Ozanam, ACS Appl. Mater. Inter. 14 (2022) 35716–35725, https://doi.org/10.1021/acsami.2c08203.
[42] S. Oswald, M. Hoffmann, M. Zier, Appl. Surf. Sci. 401 (2017) 408–413, https://doi.org/10.1016/j.apsusc.2016.12.223.

[43] J. Vacik, I. Tomandl, V. Hnatowicz, P. Horak, A. Cannavo, G. Ceccio, D. Fink, T. Kobayashi, Y. Rongbin, M. Baba, In: AIP Conference Proceedings, AIP Publishing LLC, 2019 030005, https://doi.org/10.1063/1.5127680.
[44] NIST, Certificate of Analysis Standard Reference Material 2137, 2010. https://tsapps.nist.gov/srmext/certificates/archives/2137.pdf.
[45] J. Meija, T.B. Coplen, M. Berglund, W.A. Brand, P. De Bièvre, M. Gröning, N. E. Holden, J. Irrgeher, R.D. Loss, T. Walczyk, Pure Appl. Chem. 88 (2016) 293–306, https://doi.org/10.1515/pac-2015-0503.
[46] J.F. Ziegler, M.D. Ziegler, J.P. Biersack, Nucl. Instrum. Methods Phys. Res. Sect. B Beam Interact. Mater. Atoms 268 (2010) 1818–1823, https://doi.org/10.1016/j.nimb.2010.02.091.
[47] M.A. Trunk, Determination of Isotope Concentration Profiles in Materials Science Applications Using Cold Neutrons, Dissertation, Technische Universität München, 2021.
[48] K. Jalkanen, J. Karppinen, L. Skogström, T. Laurila, M. Nisula, K. Vuorilehto, Appl. Energy 154 (2015) 160–172, https://doi.org/10.1016/j.apenergy.2015.04.110.
[49] T. Waldmann, B.-I. Hogg, M. Wohlfahrt-Mehrens, J. Power Sources 384 (2018) 107–124, https://doi.org/10.1016/j.jpowsour.2018.02.063.
[50] Q.Q. Liu, C.Y. Du, B. Shen, P.J. Zuo, X.Q. Cheng, Y.L. Ma, G.P. Yin, Y.Z. Gao, RSC Adv. 6 (2016) 88683–88700, https://doi.org/10.1039/c6ra19482f.
[51] M. Flügel, M. Bolsinger, M. Marinaro, V. Knoblauch, M. Hölzle, M. Wohlfahrt-Mehrens, T. Waldmann, J. Electrochem. Soc. 170 (2023) 060536, https://doi.org/10.1149/1945-7111/acdda3.
[52] L.M. Babcock, J. Am. Chem. Soc. 125 (2003) 12058–12059, https://doi.org/10.1021/ja033535b.
[53] B. Chapman, Glow Discharge Processes: Sputtering and Plasma Etching, Wiley, 1980.
[54] M. Parker, M.L. Hartenstein, R.K. Marcus, Spectrochim. Acta B Atom Spectrosc. 52 (1997) 567–578, https://doi.org/10.1016/S0584-8547(96)01659-X.
[55] A.B. Anfone, R.K. Marcus, J. Anal. Atomic Spectrom. 16 (2001) 506–513, https://doi.org/10.1039/b009874o.
[56] M. Wetjen, M. Trunk, L. Werner, R. Gernhauser, B. Markisch, Z. Revay, R. Gilles, H. A. Gasteiger, J. Electrochem. Soc. 165 (2018) A2340–A2348, https://doi.org/10.1149/2.1341810jes.
[57] A. Bordes, E. De Vito, C.d. Haon, A. Boulineau, A. Montani, P. Marcus, Chem. Mater. 28 (2016) 1566–1573, https://doi.org/10.1021/acs.chemmater.6b00155.
[58] N. Delpuech, N. Dupre, P. Moreau, J.S. Bridel, J. Gaubicher, B. Lestriez, D. Guyomard, ChemSusChem 9 (2016) 841–848, https://doi.org/10.1002/cssc.201501628.
[59] K. Richter, T. Waldmann, N. Paul, N. Jobst, R.-G. Scurtu, M. Hofmann, R. Gilles, M. Wohlfahrt-Mehrens, ChemSusChem 13 (2020) 529–538, https://doi.org/10.1002/cssc.201903139.
[60] N. Paul, M. Wetjen, S. Busch, H. Gasteiger, R. Gilles, J. Electrochem. Soc. 166 (2019) A1051–A1054, https://doi.org/10.1149/2.0781906jes.
[61] J. Malherbe, H. Martinez, B. Fernández, C. Pécheyran, O.F. Donard, Spectrochim. Acta B Atom Spectrosc. 64 (2009) 155–166, https://doi.org/10.1016/j.sab.2008.11.009.